

Fusion of Visual-Inertial Odometry with LiDAR Relative Localization for Cooperative Guidance of a Micro-Scale Aerial Vehicle

Václav Pritzl^{a,b}, Matouš Vrba^a, Petr Štěpán^a, Martin Saska^a

^aThe authors are with the Multi-robot Systems Group, Department of Cybernetics, Faculty of Electrical Engineering, Czech Technical University in Prague, Czech Republic, {vaclav.pritzl, matous.vrba, petr.stepan, martin.saska}@fel.cvut.cz.

^bCorresponding author

Abstract

A novel relative localization approach for cooperative guidance of a micro-scale Unmanned Aerial Vehicle (UAV) fusing Visual-Inertial Odometry (VIO) with Light Detection and Ranging (LiDAR) is proposed in this paper. LiDAR-based localization is accurate and robust to challenging environmental conditions, but 3D LiDARs are relatively heavy and require large UAV platforms. Visual cameras are cheap and lightweight. However, visual-based self-localization methods exhibit lower accuracy and can suffer from significant drift with respect to the global reference frame. We focus on cooperative navigation in a heterogeneous team of a primary LiDAR-equipped UAV and secondary camera-equipped UAV. We propose a novel cooperative approach combining LiDAR relative localization data with VIO output on board the primary UAV to obtain an accurate pose of the secondary UAV. The pose estimate is used to guide the secondary UAV along trajectories defined in the primary UAV reference frame. The experimental evaluation has shown the superior accuracy of our method to the raw VIO output and demonstrated its capability to guide the secondary UAV along desired trajectories while mitigating VIO drift.

Multimedia Attachment

<http://mrs.felk.cvut.cz/coop-fusion>

1. INTRODUCTION

Autonomous multi-rotor Unmanned Aerial Vehicles (UAVs) are well-suited for emergency response tasks in confined indoor spaces. In these applications, the UAVs operate in Global Navigation Satellite System (GNSS)-denied environments but still require accurate positioning in a world reference frame, e.g., to report victim positions, as was demonstrated in the DARPA SubT challenge [1, 2].

Camera-equipped UAVs can utilize Visual-Inertial Odometry (VIO) and may be small enough to fly through highly confined environments. However, visual-based localization approaches are heavily dependent on lighting conditions [3], the amount of texture in the environment [4], and suffer from long-term drift with respect to the world frame due to the VIO's four unobservable Degrees of Freedom (DOFs) [5]. Monocular camera-based methods exhibit scale unobservability under constant acceleration [6, 7].

Light Detection and Ranging (LiDAR)-based methods rely on the geometric structure of the environment. In comparison to visual-based methods, 3D LiDAR-based methods exhibit lower drift and perform well under challenging lighting conditions. Most of the best-performing algorithms on the KITTI dataset [8] are LiDAR-based. However, 3D LiDARs are relatively heavy, expensive, and power-consuming. Although all the teams in the DARPA SubT challenge relied on LiDARs, the

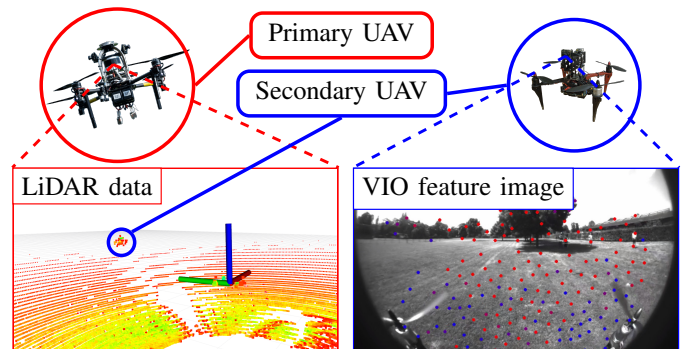


Figure 1: The primary UAV carrying a 3D LiDAR guides the secondary camera-equipped UAV using a fusion of LiDAR detections and VIO data.

UAV platforms needed for carrying such payloads are too bulky for exploring many narrow passages [9].

Using teams of UAVs with different sensors keeps the benefits of the localization methods while mitigating the disadvantages. The LiDAR-equipped UAV can share its localization data and information about the surrounding environment with the other UAVs. The camera-equipped UAV can pass through more confined spaces and cheaply extend the perception range of the UAV team due to its low cost.

We propose a novel approach to cooperative flight in GNSS-denied environments, providing accurate relative localization between the UAVs, and enabling direct guidance of less-capable UAVs by a more-capable UAV, mitigating the effects of localization drift. We focus on the case of a primary UAV utilizing 3D LiDAR-based Simultaneous Localization and Mapping

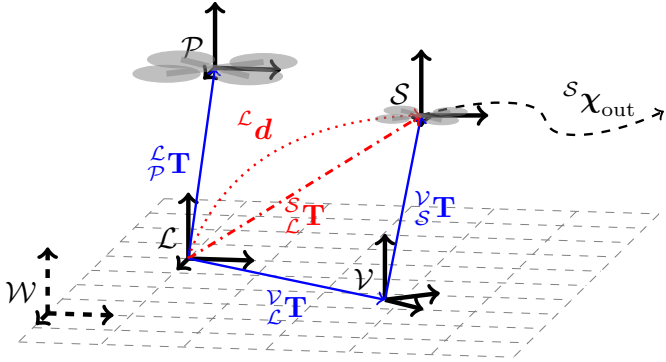


Figure 2: \mathcal{W} is the world reference frame. Frames \mathcal{P} and \mathcal{S} correspond to the primary and secondary UAV, respectively. The primary UAV is localized by LiDAR SLAM in the local frame \mathcal{L} , while the secondary UAV is localized by VIO in the local frame \mathcal{V} . The origins of frames \mathcal{L} , \mathcal{V} are at the poses where the algorithms were initialized. Frames \mathcal{L} and \mathcal{V} have 4 unobservable DOFs w.r.t. \mathcal{W} , resulting in long-term drift. Frame \mathcal{V} suffers from significantly larger drift than frame \mathcal{L} . ${}^{\mathcal{L}}\mathbf{d}$ is position of the secondary UAV detected from LiDAR data. The reference for the secondary UAV’s movement is given in the frame \mathcal{L} , transformed to ${}^{\mathcal{S}}\chi_{\text{out}}$ using the relative localization, and transmitted to the secondary UAV.

(SLAM) and a lightweight secondary UAV carrying a monocular camera utilizing VIO (see Fig. 1).

The proposed approach can enable a variety of multi-UAV tasks in GNSS-denied environments, e.g., cooperative exploration and mapping in confined, sensory-degraded spaces or correcting VIO drift of a cooperating swarm of micro-UAVs.

1.1. Notations

We denote vectors as bold lowercase letters, matrices as bold upright uppercase letters, and reference frames as uppercase calligraphic letters. Let ${}^{\mathcal{B}}\mathbf{t}$ be the vector describing the position of the origin of frame \mathcal{A} in frame \mathcal{B} . Let ${}^{\mathcal{B}}\mathbf{R} \in SO(3)$ be the rotation matrix from frame \mathcal{A} to frame \mathcal{B} . We denote

$${}^{\mathcal{B}}\mathbf{T} = \begin{bmatrix} {}^{\mathcal{B}}\mathbf{R} & {}^{\mathcal{B}}\mathbf{t} \\ \mathbf{0}^T & 1 \end{bmatrix} \in SE(3) \quad (1)$$

as the transformation matrix from frame \mathcal{A} to frame \mathcal{B} . Let ${}^{\mathcal{A}}\mathbf{x}_{[t_k]}$ be a 3D position vector in frame \mathcal{A} at time t_k . We denote ${}^{\mathcal{A}}\mathcal{D}$ as the set of LiDAR detections in reference frame \mathcal{A} and ${}^{\mathcal{A}}\chi$ as the desired UAV trajectory in frame \mathcal{A} .

1.2. Problem statement

We focus on cooperation in a heterogeneous UAV team with various localization sensors. The crucial part is fusing LiDAR relative localization with VIO ego-motion estimates for guidance of a less-capable UAV by a more-capable UAV. The more-capable *primary* UAVs carries a 3D LiDAR. The less-capable *secondary* UAV is equipped with a monocular camera. Both UAVs carry an onboard computer, a wireless communication module, a Flight Control Unit (FCU) with an embedded attitude controller, and an Inertial Measurement Unit (IMU). The UAVs operate in a GNSS-denied environment. All algorithms run fully on board the UAVs.

The problem is illustrated in Fig. 2. The first task is to estimate the transformations ${}^{\mathcal{V}}\mathbf{T}$ and ${}^{\mathcal{S}}\mathbf{T}$ to provide relative localization between the UAVs. All reference frames are aligned with the gravity vector obtained from the IMU data. Therefore we estimate 4-DOF transformations, consisting of 3D translation and relative heading.

The second task is to use the relative localization data to guide the secondary UAV along the desired trajectory ${}^{\mathcal{L}}\chi_{\text{in}}$. The aim is to, first, give the primary UAV the capability to directly guide the secondary UAV to, e.g., inspect a specific place or pass around obstacles. Second, to mitigate the effects of VIO drift to approach the trajectory tracking precision achievable with the less-drifting primary UAV localization.

Depending on the environment, the LiDAR relative localization output ${}^{\mathcal{L}}\mathbf{d}$ is subject to potential false detections and variable delay due to LiDAR data processing time. The communication between the UAVs is subject to variable delay depending on the network reliability. We assume no prior knowledge about the transformation ${}^{\mathcal{V}}\mathbf{T}$ or about the initial UAV poses. The proposed approach tries to minimize the computational and payload requirements on the secondary UAV by offloading them onto the primary UAV.

1.3. Related work

1.3.1. UAV relative localization

In unknown GNSS-denied environments, there are several ways to solve relative localization between UAVs. Marker-based visual detectors utilize markers, such as ultraviolet (UV) LEDs in combination with UV-sensitive cameras [10]. Markerless approaches typically rely on a Convolutional Neural Network (CNN) [11, 12, 13]. Machine learning-based techniques are susceptible to changes in the appearance of the targets and the environment. Vision-based approaches struggle under low visibility and fail to provide precise 3D position estimates due to inaccurate distance estimation [12].

Equipping the UAVs with Ultra-wideband (UWB) modules provides distance measurements between pairs of the modules [14]. The overall localization accuracy is highly dependent on the shape and size of the UAV formation, as it may suffer from unobservabilities and dilution of precision.

A multi-robot SLAM method can obtain the relative poses through map merging and inter-robot loop closures, utilizing, e.g., LiDAR data [15, 16], stereo camera data [17], or monocular camera data [18]. Such approaches require communicating significant amounts of data or making compromises between the amount of shared data and contained information, influencing the accuracy of the localization [19]. Often, they use a ground station for computations, but we aim to run everything on board the computationally-constrained UAV platforms.

3D LiDAR data can be used for direct detection of cooperating robots. In [20], a fusion of 3D LiDAR, fisheye camera, and UWB data was used for tracking a UAV flying above a LiDAR- and camera-equipped Unmanned Ground Vehicle (UGV), with the UAV wirelessly sharing IMU and 1D LiDAR data. In [21], a decentralized LiDAR-inertial swarm odometry was proposed, utilizing direct detections of cooperating UAVs from reflectivity values of LiDAR data.

1.3.2. Cooperative navigation improving UAV localization

Our approach is similar to methods for improving localization in GNSS-challenging environments, where UAVs with reliable GNSS-based localization share data with another UAV in a GNSS-challenging area [22, 23]. These approaches utilized visual tracking for relative localization.

Using the relative localization data, we aim to improve the navigation performance of a UAV utilizing visual-based self-localization. Such a goal can be achieved by fusion with UWB measurements. For a single-UAV case, a fusion of data from static UWB anchors, LiDAR odometry, IMU, and VIO was proposed in [24]. However, placing static UWB anchors in the area is not viable in an emergency scenario. The use of multiple robots, each carrying a UWB module, decreases the dependence on external infrastructure. Such approaches fusing UWB and VIO were proposed in [25] for collaborative localization of two UAVs and in [26] for distributed formation estimation in large UAV swarms.

In [27], the authors fused the detections from a CNN with UWB data and VIO for relative localization in a UAV swarm. The same authors fused map-based inter-UAV loop-closures in [28]. Zhang et al. [29] fused active visual-based relative localization with UWB and VIO data for formation control of a marker-equipped UAV swarm. The authors of [30] focused on collaborative localization of a UGV-UAV team. Their approach relied mainly on UWB and VIO data with 3D LiDAR detections utilized during initialization.

The authors of [31] utilized a heterogeneous team of LiDAR-carrying UGVs and camera-equipped UAVs with the goal of detecting the UGVs from onboard cameras on UAVs and using them as landmarks for improving the UAV localization. Their work focused mainly on the optimal placement of the UGVs in the environment. In contrast, we focus on a heterogeneous UAV-only team with the LiDAR-carrying UAV detecting the camera-equipped UAV.

1.3.3. VIO drift mitigation

In [32], VIO drift was mitigated by finding feature correspondences in VIO data and prior LiDAR maps. Our approach does not require prior maps and can be deployed in previously unseen environments. In GNSS-enabled environments, VIO drift can be corrected by fusing raw Doppler velocities and pseudoranges [33] or 3D GNSS positions [34]. In [34], the authors obtained the GNSS-VIO frame transformation using window-based optimization and transformed the VIO state to the GNSS frame during initialization to avoid unobservabilities. The GNSS data are in the global frame but suffer from short-term meter-level drift. LiDAR data are in a local frame, resulting in minor long-term drift w.r.t. global frame, but exhibit centimeter-level precision. Our approach uses window-based optimization not only for initialization but during the entire estimation process.

In [35, 36], the authors focused on VIO and visual target tracking, improving the performance of both thanks to their tight coupling. We instead improve the navigation performance of a VIO-using UAV by guiding it by another UAV with

less-drifting localization. We opted for a loosely-coupled approach to mitigate issues with modeling errors hurting the performance, which can be more pronounced in a tightly-coupled estimator [36], and to enable our approach to be universally usable with any VIO algorithm.

1.3.4. Contributions

Each cooperative navigation approach suffers from the drawbacks of its relative localization method. Our method can accurately obtain 3D positions of UAVs without prior knowledge of their size or any visual markers. It is robust to low illumination due to the nature of the LiDAR sensor and does not require any additional hardware apart from the 3D LiDAR. Our approach poses minimal requirements on the secondary UAV, making the method compatible with a number of commercially-available UAVs and state-of-the-art VIO algorithms. It requires no prior information about the initial UAV poses.

To the best of our knowledge, the proposed approach is the first solution to relative localization between heterogeneous UAVs based on LiDAR and VIO fusion. As shown in the experimental evaluation, such a setup provides accurate localization between the UAVs and enables precise guidance of the secondary UAV with drifting VIO. In a practical application, the proposed approach can be employed not only for guiding UAVs with minimal sensory payload under constant visibility but also for guiding less-capable UAVs through areas of sensory degradation. The raw data from our real-world experiments have been released online to provide data useful for developing similar relative localization approaches to the research community.

The contributions of this work can be summarized as:

- a cooperative guidance approach enabling tracking desired trajectories defined in the primary UAV reference frame while mitigating VIO drift;
- a novel approach to UAV relative localization based on a fusion of LiDAR and VIO ego-motion data, which provides a common reference frame for a team of heterogeneously localized UAVs;
- a method for accurately estimating the time-varying relative transformation between the different reference frames of the UAVs, able to quickly react to the coordinate frame drift while taking into account possible false detections and measurement delays.

2. MULTI-UAV SYSTEM ARCHITECTURE

The architecture of the approach (see Fig. 3) is based upon the results of our preliminary work [38], which assessed the feasibility of using raw LiDAR detections to guide a cooperating UAV to desired positions. The UAV pair forms a closed feedback loop controlling the secondary UAV pose in the frame \mathcal{L} . High-level planning and estimation run on board the primary UAV. The secondary UAV receives the desired trajectories ${}^S\chi_{\text{out}}$ and tracks references in its local frame \mathcal{V} . The UAV pair is time-synchronized over the wireless network. This paper focuses mainly on the *UAV guider* module (see Fig. 4). The

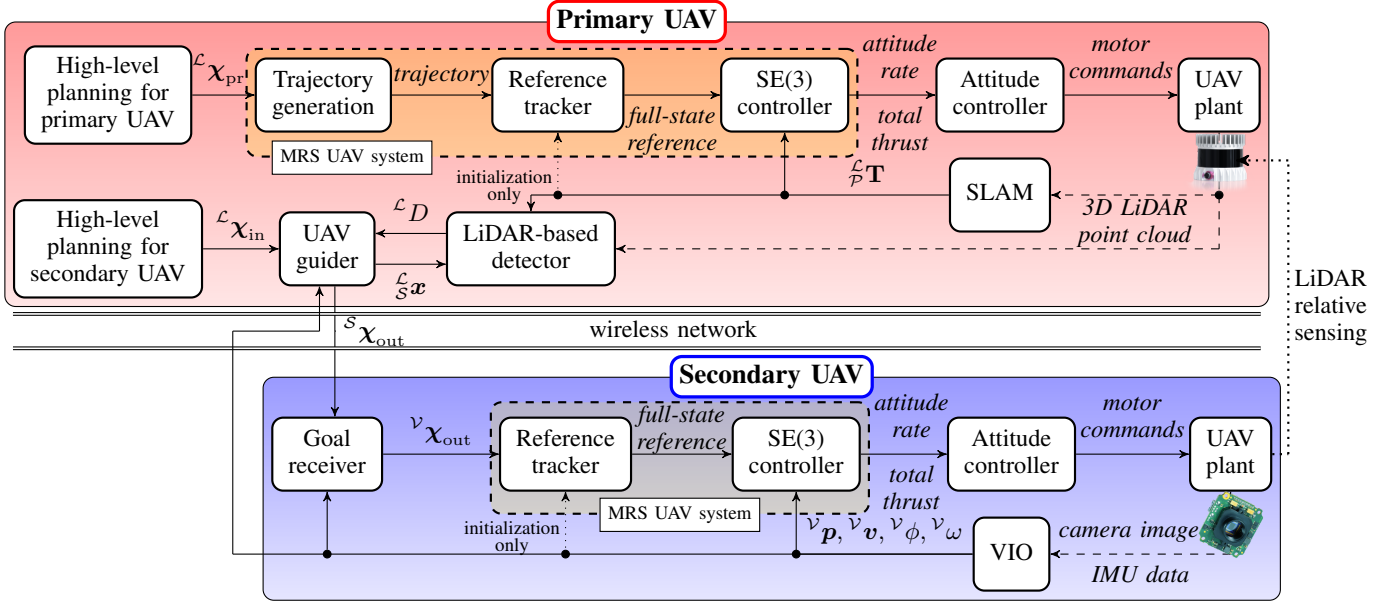


Figure 3: The primary UAV tracks the pose of the secondary UAV from the fusion of LiDAR and VIO data and transmits commands to the secondary UAV over a wireless network. Movement of the UAV pair is planned on board the primary UAV. Position control in the frame of each respective self-localization method is provided by the MRS UAV System [37].

control pipeline used for tracking references in the local frames of each self-localization method is provided by the MRS UAV System [37]¹.

2.1. LiDAR-based detector

The *LiDAR-based detector* performs multi-target detection and tracking of flying objects in the 3D LiDAR point clouds in frame \mathcal{L} . The LiDAR data processing is based on our work on autonomous interception of intruder UAVs [39, 40].

The detector constructs a voxel-based occupancy map of the surrounding environment from LiDAR data and detects flying objects in the map. A Kalman filter-based point cluster-tracking approach is utilized to compensate for the uncertainty in the sensory data and mitigate delays caused by the processing time of the detection algorithm. Here, we describe the differences employed for its use in the proposed cooperative localization and guidance approach and encourage the reader to look into [40] for more details about the *LiDAR-based detector* itself.

The *LiDAR-based detector* additionally receives the estimated UAV position ${}^{\mathcal{L}}\mathbf{x}$ from the *UAV guider* module. The position is used in cluster-to-target association instead of the tracked target position if ${}^{\mathcal{L}}\mathbf{x}$ is located within a desired uncertainty radius from a tracked target. The position ${}^{\mathcal{L}}\mathbf{x}$ can be more accurate due to the incorporation of the low-delay VIO data. The detected 3D positions of all tracked objects are sent to the *UAV guider module* in the set of detections ${}^{\mathcal{L}}D$.

2.2. UAV guider

The *UAV guider* (see Fig. 4) estimates the transformation ${}^{\mathcal{S}}\mathbf{T}$ from the LiDAR detections and VIO data, and transforms

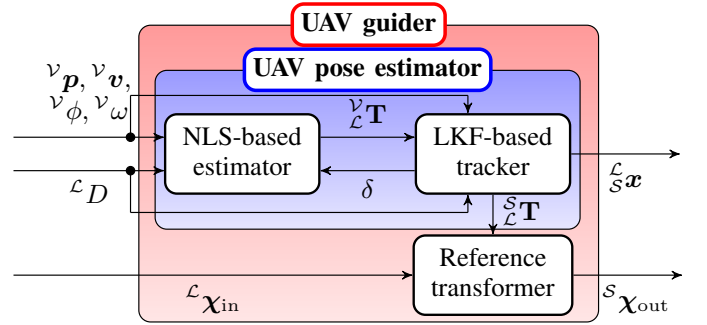


Figure 4: The UAV guider module fuses LiDAR detections with VIO data to estimate 4-DOF poses of the secondary UAV. The estimation result is used for transformation of references to the coordinate frame of the secondary UAV.

the desired trajectories to the secondary UAV's frame \mathcal{S} . The UAV pose is estimated in two loosely-coupled steps. The *Non-linear Least Squares (NLS)-based estimator* aligns LiDAR detections and VIO poses in a sliding window to produce ${}^{\mathcal{V}}\mathbf{T}$. The transformation ${}^{\mathcal{V}}\mathbf{T}$ connects the reference frames but lags behind the true transformation values in areas with large VIO drift. Therefore, the *Linear Kalman Filter (LKF)-based tracker* utilizes ${}^{\mathcal{V}}\mathbf{T}$ and fuses the latest LiDAR detections and VIO to provide a drift-compensated estimate of ${}^{\mathcal{S}}\mathbf{T}$ usable for transformation of the desired trajectories. The *LKF-based tracker* also deals with measurement delays and provides association of LiDAR detections based on their Mahalanobis distance.

¹https://github.com/ctu-mrs/mrs_uav_system

2.2.1. NLS relative transformation optimization

The 4-DOF transformation between the LiDAR SLAM frame \mathcal{L} and the VIO frame \mathcal{V} is defined as

$${}_{\mathcal{L}}^{\mathcal{V}}\mathbf{T} = \begin{bmatrix} {}_{\mathcal{L}}^{\mathcal{V}}\mathbf{R}(\theta) & {}_{\mathcal{L}}^{\mathcal{V}}\mathbf{t} \\ \mathbf{0}^T & 1 \end{bmatrix} \in SE(3). \quad (2)$$

The problem of estimating its parameters from a set of LiDAR-VIO pose correspondences in a sliding window can be formulated as

$${}_{\mathcal{L}}^{\mathcal{V}}\hat{\mathbf{t}}, \hat{\theta} = \arg \min_{{}_{\mathcal{L}}^{\mathcal{V}}\mathbf{t}, \theta} \frac{1}{2} \sum_i \rho \left(\left\| {}_{\mathcal{L}}^{\mathcal{V}}\mathbf{R}(\theta) {}_{\mathcal{L}}^{\mathcal{V}}\mathbf{d}_{[t_i]} + {}_{\mathcal{L}}^{\mathcal{V}}\mathbf{t} - {}_{\mathcal{L}}^{\mathcal{V}}\mathbf{p}_{[t_i]} \right\|^2 \right), \quad (3)$$

$${}_{\mathcal{L}}^{\mathcal{V}}\mathbf{t} \in \mathbb{R}^3, \theta \in [-\pi, \pi], \quad (4)$$

where ${}_{\mathcal{L}}^{\mathcal{V}}\mathbf{t}$ is the relative translation vector between the reference frames, θ is the relative heading, ${}_{\mathcal{L}}^{\mathcal{V}}\mathbf{d}_{[t_i]}$ is the LiDAR detection position at time t_i , and ${}_{\mathcal{L}}^{\mathcal{V}}\mathbf{p}_{[t_i]}$ is the corresponding VIO position. $\rho(\cdot)$ denotes the loss function used for reducing the influence of outliers on the optimization solution. In the experimental evaluation of the proposed approach, the Levenberg-Marquardt algorithm, implemented in the Ceres Solver [41], was employed for solving the NLS problem. The soft L1 loss function, defined as

$$\rho(s) = 2 \left(\sqrt{1+s} - 1 \right), \quad (5)$$

was employed, and the automatic differentiation functionality of the Ceres Solver was used to solve the problem.

The length of the sliding window is constant and predefined. The formulation of the optimization problem assumes constant ${}_{\mathcal{L}}^{\mathcal{V}}\mathbf{T}$ over the course of the sliding window. The LiDAR detections exhibit high accuracy with little long-term drift. The VIO positions exhibit significant long-term drift, especially in texture-less environments. Therefore, a longer window does not necessarily equal a better estimate. The window length must balance between measurement noise mitigation and long-term drift tracking. The optimal length selection may change with the environment, e.g., in an environment with a lot of features and little VIO drift, the window can be longer, whereas in a feature-less environment with significant VIO drift, a shorter window is desired.

The LiDAR-VIO correspondence set $\left\{ \left[{}_{\mathcal{L}}^{\mathcal{V}}\mathbf{d}_{[t_i]}, {}_{\mathcal{L}}^{\mathcal{V}}\mathbf{p}_{[t_i]} \right]_i \right\}$ is constructed from the VIO position buffer by linearly interpolating the LiDAR detections to time stamps corresponding to each VIO position in the buffer. The result of the NLS optimization is only used if the optimization converges and its final cost is lower than a predefined threshold.

2.2.2. LKF-based tracker

The LKF-based tracker predicts the state of the secondary UAV in the frame \mathcal{L} and outputs the estimated UAV position ${}_{\mathcal{L}}^{\mathcal{L}}\mathbf{x}$ and matrix ${}_{\mathcal{L}}^{\mathcal{L}}\mathbf{S}$ used for transforming the desired references for secondary UAV.

The tracker is based on an LKF with a recalculating history buffer [42]. The history buffer contains recent measurements and measurement covariance matrices sorted by time stamps.

When the tracker predicts its state at a specific time, it is calculated using information from the oldest element in the buffer up to the desired time stamp. The tracker is based upon a 4-DOF constant-velocity model with a state vector

$$\mathbf{x}^{\text{KF}} = \begin{bmatrix} {}_{\mathcal{L}}^{\mathcal{L}}\mathbf{x}^T & {}_{\mathcal{L}}^{\mathcal{L}}\mathbf{v}^T & {}_{\mathcal{L}}^{\mathcal{L}}\phi & {}_{\mathcal{L}}^{\mathcal{L}}\omega \end{bmatrix}_{8 \times 1}^T, \quad (6)$$

where ${}_{\mathcal{L}}^{\mathcal{L}}\mathbf{x}$ is the 3D position of the secondary UAV in the LiDAR SLAM frame, ${}_{\mathcal{L}}^{\mathcal{L}}\mathbf{v}$ is the velocity of the UAV, ${}_{\mathcal{L}}^{\mathcal{L}}\phi$ is the heading, and ${}_{\mathcal{L}}^{\mathcal{L}}\omega$ is the heading rate. The measurement vectors used for updating the estimate are

$$\mathbf{z}_{\mathcal{L}}^{\text{KF}} = \begin{bmatrix} {}_{\mathcal{L}}^{\mathcal{L}}\mathbf{d} \end{bmatrix}_{3 \times 1}, \mathbf{z}_{\mathcal{V}}^{\text{KF}} = \begin{bmatrix} z_x^T & z_v^T & z_\phi & z_\omega \end{bmatrix}_{8 \times 1}^T, \quad (7)$$

where $\mathbf{z}_{\mathcal{L}}^{\text{KF}}$ is constructed each time a new LiDAR detection ${}_{\mathcal{L}}^{\mathcal{L}}\mathbf{d}$ is associated to the estimate \mathbf{x}^{KF} . If the latest VIO pose from time t_l is newer than the latest LiDAR measurement from time t_k , the measurement vector $\mathbf{z}_{\mathcal{V}}^{\text{KF}}$ is used, with the position measurement calculated as

$$\mathbf{z}_{\mathcal{V}[t_l]} = {}_{\mathcal{L}}^{\mathcal{L}}\mathbf{d}_{[t_k]} + {}_{\mathcal{L}}^{\mathcal{V}}\mathbf{R}(\theta) \left({}_{\mathcal{L}}^{\mathcal{V}}\mathbf{p}_{[t_l]} - {}_{\mathcal{L}}^{\mathcal{V}}\mathbf{p}_{[t_k]} \right), \quad (8)$$

where ${}_{\mathcal{L}}^{\mathcal{L}}\mathbf{d}_{[t_k]}$ is the latest LiDAR detection, ${}_{\mathcal{L}}^{\mathcal{V}}\mathbf{p}_{[t_l]}$ is the new VIO pose, ${}_{\mathcal{L}}^{\mathcal{V}}\mathbf{p}_{[t_k]}$ is the VIO pose interpolated to time t_k , and ${}_{\mathcal{L}}^{\mathcal{V}}\mathbf{R}(\theta)$ is the rotation matrix constructed from the latest NLS optimization output. The velocity measurement is calculated as

$$\mathbf{z}_{\mathcal{V}[t_l]} = {}_{\mathcal{L}}^{\mathcal{V}}\mathbf{R}(\theta) {}_{\mathcal{L}}^{\mathcal{V}}\mathbf{v}_{[t_l]}, \quad (9)$$

where ${}_{\mathcal{L}}^{\mathcal{V}}\mathbf{v}_{[t_l]}$ is the velocity obtained from the VIO. The heading and heading rate measurements are constructed as

$$\mathbf{z}_{\phi[t_l]} = {}_{\mathcal{L}}^{\mathcal{V}}\phi_{[t_l]} - \theta, \mathbf{z}_{\omega[t_l]} = {}_{\mathcal{L}}^{\mathcal{V}}\omega_{[t_l]}, \quad (10)$$

where ${}_{\mathcal{L}}^{\mathcal{V}}\phi_{[t_l]}$ is the heading of the VIO pose, θ is the relative heading obtained from the NLS optimization, and ${}_{\mathcal{L}}^{\mathcal{V}}\omega_{[t_l]}$ is the heading rate from the VIO output. If the received VIO pose is older than the latest LiDAR measurement, only the heading and heading rate states are updated with the measurement vector constructed as

$$\mathbf{z}_{\phi}^{\text{KF}} = \begin{bmatrix} z_\phi & z_\omega \end{bmatrix}_{2 \times 1}^T, \quad (11)$$

where its elements are calculated by equation (10).

New LiDAR detections are associated to the estimate \mathbf{x}^{KF} based on their Euclidean and Mahalanobis distance. If the Euclidean distance of a detection from the estimate is lower than a predefined threshold, its squared Mahalanobis distance from the estimate at the corresponding time is calculated as

$$\delta_{[t_k]}^2 = \mathbf{y}_{[t_k]}^T \mathbf{S}_{[t_k]}^{-1} \mathbf{y}_{[t_k]}, \quad (12)$$

where $\mathbf{y}_{[t_k]}$ is the measurement innovation and $\mathbf{S}_{[t_k]}$ is the innovation covariance calculated during the LKF correction. The detection with the lowest distance $\delta_{[t_k]}$ is selected. If the detection is consistent with the LKF state, $\delta_{[t_k]}^2$ should be characterized by the χ^2 distribution. The estimator performs a hypothesis test by comparing $\delta_{[t_k]}^2$ to a critical value $\chi^2(p, m)$ with a desired

p -value and m DOFs, where m is the dimension of the measurement vector. The LKF-based tracker assumes the modeled process and the incoming measurements are subject to zero-mean white Gaussian noise. The noise of the LiDAR detections depends on a number of factors, including the LiDAR parameters, range to the target, and noise in the sensor pose itself [40]. Incorrect modeling of the measurement noise may result in inconsistent performance, causing divergence from the true state and rejection of valid measurements. To achieve consistent performance, the noise values are empirically tuned based on real-world experimental data to make sure that the squared Mahalanobis distance $\delta_{[t_k]}^2$ of valid measurements follows the χ^2 distribution for the desired confidence level.

2.2.3. Estimate initialization

The *LiDAR-based detector* provides a set of detections ${}^{\mathcal{L}}D$ of all the tracked flying objects in the surrounding environment. The *UAV pose estimator* constructs a separate detection buffer for each tracked object and performs the NLS trajectory alignment (eq. (3)) for each detection buffer and the VIO pose buffer. If the buffers contain sufficient movement of the UAV and the NLS optimization converges to a solution with the final cost below a specified threshold, the estimate is initialized based on this detection buffer.

2.2.4. Reference transformer

The *Reference transformer* utilizes the relative transformation ${}^{\mathcal{S}}\mathbf{T}$ produced by the estimator to transform the desired trajectory ${}^{\mathcal{L}}\chi_{\text{in}}$ to the secondary UAV reference frame \mathcal{S} . The reference transformer keeps track of what part of the desired trajectory has already been completed in order to transmit only unvisited parts and repeatedly transmits references to the secondary UAV at the rate of 5 Hz. On board the secondary UAV, the *Goal receiver* module receives the trajectories and checks them for time stamp inconsistencies before transferring them to the secondary UAV control pipeline.

2.3. Analysis of degenerate cases

In the proposed approach, these degenerate cases can arise:

2.3.1. Loss of LiDAR detections ${}^{\mathcal{L}}d$

When line-of-sight visibility between the UAVs gets broken, the transformations ${}^{\mathcal{S}}\mathbf{T}$ and ${}^{\mathcal{V}}\mathbf{T}$ become unobservable. The estimator will keep tracking the UAV from the VIO poses transformed using the latest ${}^{\mathcal{V}}\mathbf{T}$ (see eq. (7)-(10)), but the estimated UAV pose in the frame \mathcal{L} will drift away from its true value, as ${}^{\mathcal{V}}\mathbf{T}$ will not be getting updated. When visibility between the UAVs gets re-established, the estimate will be corrected or re-initialized.

2.3.2. Loss of VIO poses ${}^{\mathcal{V}}p$

When communication between the UAVs gets broken, its 3D position ${}^{\mathcal{L}}\mathbf{x}$ is still observable from the LiDAR data, but the transformation ${}^{\mathcal{V}}\mathbf{T}$ and the heading ${}^{\mathcal{L}}\phi$ of the secondary UAV become unobservable. The estimator will keep tracking the UAV but will not update the ${}^{\mathcal{L}}\phi$ and ${}^{\mathcal{L}}\omega$ states during the loss of communication.

2.3.3. Small translational motion of the secondary UAV

The relative transformation ${}^{\mathcal{V}}\mathbf{T}$ becomes unobservable as the UAV trajectory in the sliding window degrades to a single point. If the observed UAV motion falls to the level of the LiDAR measurement noise, the resulting estimate will become inconsistent. Such a situation is detected based on the trajectory length in the window and the eigenvalues of the Fisher information matrix

$$\mathbf{F}({}^{\mathcal{V}}\hat{\mathbf{t}}, \hat{\theta}) = \mathbf{J}({}^{\mathcal{V}}\hat{\mathbf{t}}, \hat{\theta})^T \mathbf{J}({}^{\mathcal{V}}\hat{\mathbf{t}}, \hat{\theta}), \quad (13)$$

constructed from the Jacobian \mathbf{J} evaluated when solving the NLS problem. As the optimization problem becomes degenerate, the lowest eigenvalue of the matrix \mathbf{F} tends to zero. If the eigenvalue falls below a predefined threshold, the estimator stops updating ${}^{\mathcal{V}}\mathbf{T}$.

3. EXPERIMENTAL VERIFICATION

Video of the experimental verification is available online ².

3.1. Simulations

3.1.1. Drift compensation

Simulations in the Gazebo simulator were performed to evaluate the ability to compensate for the odometry drift. The simulations were performed in an indoor environment with no obstacles breaking the line of sight between the UAVs (see the multimedia attachment). In the simulated scenario, the primary UAV moved in a 3 by 3 m large square while guiding the secondary UAV to follow a surrounding circular trajectory with the radius of 4 m at the velocity of 0.5 m s⁻¹ (see Fig. 5). The trajectories were predefined in the LiDAR SLAM reference frame. In each run of the simulation, the secondary UAV was tasked to complete the circle 10 times.

The primary UAV carried a simulated LiDAR with the same parameters as its real-world counterpart from Sec. 3.2 and utilized it in the LOAM [43] SLAM algorithm. Instead of real VIO, the secondary UAV control loop used ground-truth localization with artificially inserted constant-velocity drift in the x -axis. The approach was evaluated for drift values ranging from 0 to 1 m s⁻¹ with the step of 0.1 m s⁻¹. For each drift value, the simulation was done 10 times. The simulation run was considered to be a failure, if the secondary UAV failed to complete the 10 circles, e.g., due to collision with the surrounding obstacles.

Fig. 6 shows the mean deviation from the circular path, the Root Mean Squared Error (RMSE) of the relative localization, and the number of runs in which the UAV failed to complete the 10 circles. The simulations were completely successful for drift values up to 0.7 m s⁻¹ with one failure for the drift of 0.8 m s⁻¹. The mean path deviation ranged from 0.14 m in the case of zero drift up to 0.67 m in the case of 0.8 m s⁻¹ drift. The relative localization RMSE ranged from 0.08 m up to 0.48 m.

²<http://mrs.felk.cvut.cz/coop-fusion>

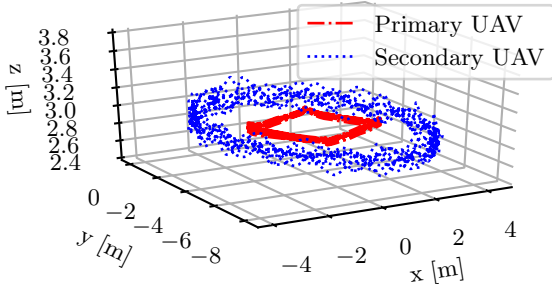


Figure 5: Trajectories in the simulation with zero drift.

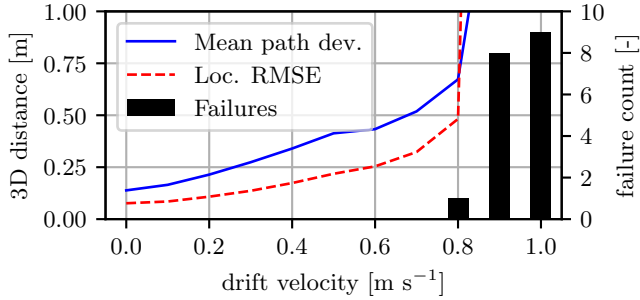


Figure 6: Mean deviation from the circular path, relative localization RMSE, and failure count for each drift value.

3.1.2. Non-Line-of-Sight (NLOS) simulation

The approach was evaluated in a simulated NLOS situation. The primary UAV moved back and forth in a line and guided the secondary UAV to follow a trajectory passing through a 1 m wide gap and behind a wall (see Fig. 8). The secondary UAV was 0.45 m × 0.45 m wide including propellers. The secondary UAV performed the loop 10 times. Two additional UAVs hovered next to the desired trajectory to demonstrate the robustness of the approach to false detections. As in the previous simulation, the primary UAV carried a simulated Ouster OS0-128 3D LiDAR with the LiDAR data utilized by the LOAM [43] SLAM. The secondary UAV carried a fisheye camera with IMU corresponding to those used in the real-world experiments and utilized VINS-Mono [44] in its control loop.

Fig. 9 shows the progression of the localization error of the proposed fusion approach with respect to the ground truth. When the visibility was lost, the localization started drifting but was corrected each time when the visibility was re-established. The position RMSE was 0.11 m when the UAV was tracked by the primary UAV (calculated from the localization data obtained at the time periods when the secondary UAV was detected in the LiDAR data) and 0.35 m when it was out of sight.

3.2. Real-world evaluation

To the best of the authors' knowledge, there are not yet any standard datasets containing multiple UAVs with LiDAR data and heterogeneous localization methods, usable for testing such an approach, as proposed in this paper. Therefore, the raw data from the real-world flights performed in this work have been released online³ to enable reproducibility of our results

³https://github.com/ctu-mrs/coop_uav_dataset

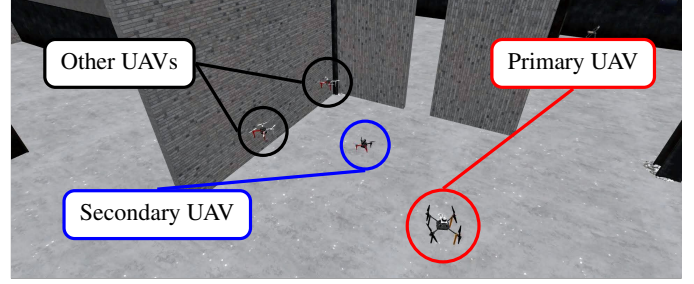


Figure 7: NLOS experiment in the Gazebo simulator.

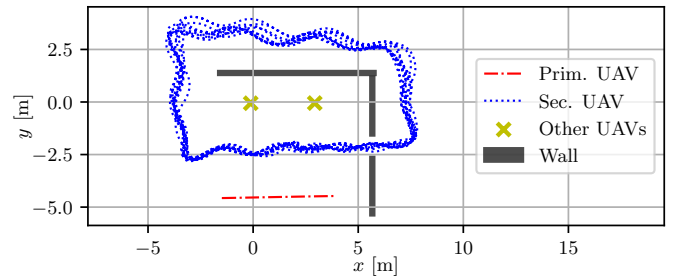


Figure 8: Ground-truth trajectories from NLOS simulation.

and provide data useful for developing such relative localization approaches to the research community.

3.2.1. Experimental setup

The UAV platforms are shown in Fig. 10. For a detailed description of the UAV hardware, see [45, 46]. The primary UAV is built upon the X500 frame and carries the Intel NUC 10i7FNH onboard computer with the Intel Core i7 10710U CPU, 16 GB of RAM, and a Wi-Fi module. The secondary UAV is built upon the F330 frame and carries the Intel NUC 8i7BEH with the Intel Core i7-8559U CPU and 16 GB RAM. Both UAVs carry the Pixhawk 4 FCU containing the embedded attitude controller.

The primary UAV carries the Ouster OS0-128 Rev C 3D LiDAR. The LiDAR weighs 430 g without its top radial cap, has a 360° horizontal and 90° vertical Field Of View (FOV), and produces scans with the resolution of 1024 × 128 beams at a rate of 10 Hz. The primary UAV utilizes the LOAM SLAM algorithm [43] for its self-localization.

The secondary UAV carries the front-facing Bluefox MLC200Wc camera with the DSL217 fisheye lens. The camera is rigidly connected to the ICM-42688-P IMU. The camera produces images at the rate of 30 Hz at 752 × 480 resolution. For self-localization, the secondary UAV utilizes the VINS-Mono algorithm [44] with disabled loop closure detection. The VINS-Mono algorithm processes the images at the rate of 10 Hz and the IMU at the rate of 1000 Hz. The UAV is equipped with the Emlid Reach Real-time kinematic (RTK) module for ground truth recording.

The software on board the UAVs is based on Ubuntu 20.04, Robot Operating System (ROS) 1, and the MRS UAV system [37]. Nimbro network is used for transporting the ROS topics over the wireless network. The system time of the onboard

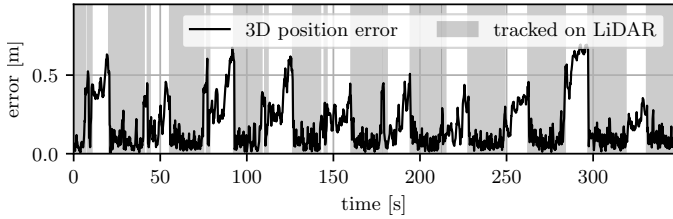


Figure 9: Relative localization error from NLOS simulation.

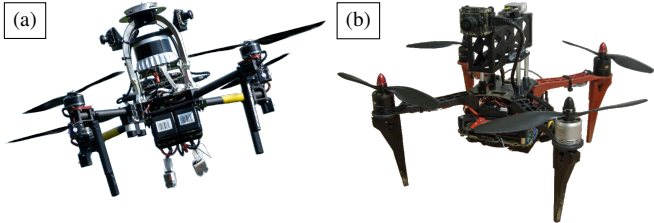


Figure 10: UAV platforms employed in the real-world experiments: (a) primary UAV carrying the Ouster 3D LiDAR, (b) secondary UAV with the monocular camera.

computers of the UAVs is synchronized using *chrony*⁴ with the primary UAV acting as a server and the secondary UAV acting as a client. All algorithms ran entirely on board the UAVs. The RTK data were collected for offline ground truth comparison and were not utilized in the control loop of the UAVs in any way.

The ground truth comparison was performed based on the trajectory evaluation methods described in [47]. Each evaluated trajectory was aligned with the RTK ground truth data based on the first 20 seconds of each data series. The error at each data point was calculated as the Euclidean distance between the aligned trajectory and the ground truth. For each trajectory, the 2D and 3D Absolute Trajectory Errors (ATEs) were calculated as the total RMSE between the ground truth and the aligned trajectory.

3.2.2. Results

The secondary UAV trajectory was predefined in the LiDAR SLAM frame, and the primary UAV guided the secondary UAV to follow the trajectory based on its commands. Two trajectories were evaluated: a circle with 0.5 m s^{-1} velocity and a figure eight with 1 m s^{-1} velocity. The UAV faced the direction of its movement. The primary UAV was commanded by an operator to keep changing its pose while being stabilized based on its LiDAR localization. In the circular flight, the mutual UAV distance ranged between 3.2–10.9 m with a mean of 7.0 m. In the figure-eight flight, the distance ranged between 2.5–9.8 m with a mean of 6.3 m. The algorithms proved capable of real-time usage on board the UAVs with the LiDAR-based detector producing detections at the rate of 10 Hz and the fusion algorithm taking less than 5 ms to fuse them to produce each estimate.

The data from flights, aligned to a common reference frame, are shown in Fig. 12. In both cases, the VIO output exhibited significant drift, mainly in the direction of the z -axis. Despite

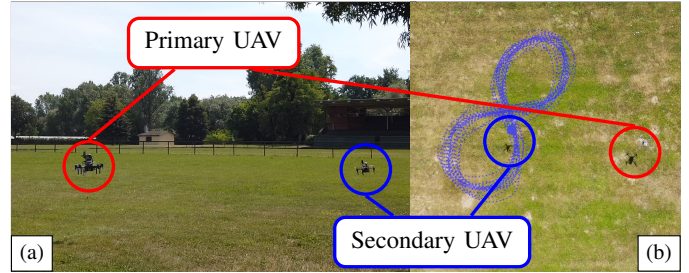


Figure 11: Side view (a) and top-down view (b) of the experimental verification. Ground-truth trajectory of the secondary UAV is drawn over the image.

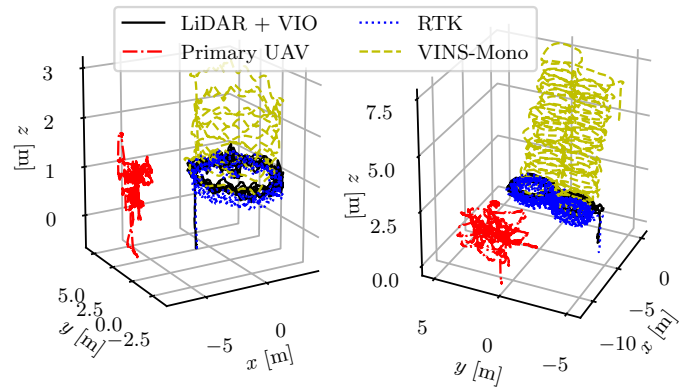


Figure 12: Trajectories from the real-world flights.

the drift, the proposed method accurately tracked the secondary UAV and enabled correct guidance of the UAV along the desired trajectories. Fig. 13 compares the localization error of the LiDAR + VIO fusion, VINS-Mono, and OpenVINS. OpenVINS [48] was run offline using the collected data for error comparison. While the output of the VIO methods was constantly drifting, the error of the LiDAR + VIO fusion was unaffected by this drift. The data shows that drift between two VIO methods can significantly differ, even if they use the same data, making the drift values difficult to estimate beforehand. Furthermore, the amount of drift can change with texture in the scene, illumination, propeller-induced vibrations picked up by the IMU, etc.

Table 1 contains the ATEs of the LiDAR + VIO fusion and the tested VIO methods. Both the 3D error and the 2D error in the xy -plane are provided, as the VINS-Mono drift was most significant in the z -axis, and the LiDAR vertical resolution is lower than its horizontal resolution. The 3D ATE of the LiDAR + VIO fusion was 0.19 m in the circular flight and 0.36 m in the figure-eight flight, significantly lower than the errors of the VIO output. The fusion error in the figure-eight flight was larger than that of the circular flight due to the greater velocity of the secondary UAV. The experimental evaluation showed that guidance based on the LiDAR + VIO fusion is capable of mitigating the effects of the VIO drift on the flight of the secondary UAV.

⁴<https://chrony.tuxfamily.org>

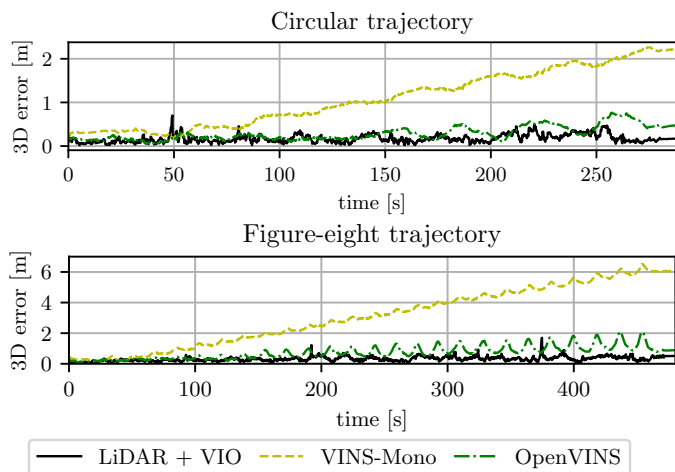


Figure 13: Progression of 3D localization error over time from both of the performed trajectories. The error was calculated as the Euclidean distance between the RTK ground truth and the respective aligned trajectory.

Trajectory	LiDAR + VIO		VINS-Mono		OpenVINS	
	2D	3D	2D	3D	2D	3D
circle	0.13	0.19	0.49	1.21	0.28	0.32
eight	0.22	0.36	1.44	3.55	0.68	0.83

Table 1: Overall ATEs in meters, calculated as the RMSE of all aligned data points.

4. CONCLUSIONS

An approach for cooperative guidance of a micro-scale UAV relying on a novel technique of relative localization was proposed in this paper. We proposed a heterogeneous UAV team consisting of a LiDAR-equipped primary UAV and a small camera-equipped secondary UAV, combining the benefits of both sensor types. To achieve the desired tight cooperation of UAVs with different sensory modalities, we proposed a novel approach for fusing the LiDAR relative localization with VIO output on board the primary UAV to obtain accurate pose of the secondary UAV. We demonstrated that the resulting pose estimate can be used to guide the secondary UAV along desired trajectories defined in the reference frame of the primary UAV. The performance of the proposed approach was verified and quantitatively evaluated in simulations and real-world experiments. The results showed the superior accuracy of the fusion output to the pure VIO data and successfully demonstrated the capability to guide the secondary UAV along the desired trajectories.

References

[1] M. Petrlik, P. Petracek, V. Kratyk, T. Musil, Y. Stasinchuk, M. Vrba, T. Baca, D. Hert, M. Pecka, T. Svoboda, M. Saska, UAVs Beneath the Surface: Cooperative Autonomy for Subterranean Search and Rescue in DARPA SubT, arXiv:2206.08185 [cs] (Jun. 2022). doi:10.48550/arXiv.2206.08185.

[2] V. Krátký, P. Petráček, T. Báča, M. Saska, An autonomous unmanned aerial vehicle system for fast exploration of large complex indoor environments, JFR 38 (8) (2021) 1036–1058. doi:10.1002/rob.22021.

[3] J. Bednar, M. Petrlik, K. C. Teixeira Vivaldini, M. Saska, Deployment of Reliable Visual Inertial Odometry Approaches for Unmanned Aerial Vehicles in Real-world Environment, in: ICUAS, IEEE, 2022.

[4] H. Lim, Y. Kim, K. Jung, S. Hu, H. Myung, Avoiding Degeneracy for Monocular Visual SLAM with Point and Line Features, in: IEEE ICRA, 2021. doi:10.1109/ICRA48506.2021.9560911.

[5] J. A. Hesch, D. G. Kottas, S. L. Bowman, S. I. Roumeliotis, Consistency Analysis and Improvement of Vision-aided Inertial Navigation, IEEE T-RO 30 (1) (2014) 158–176. doi:10.1109/TR0.2013.2277549.

[6] K. J. Wu, S. I. Roumeliotis, Unobservable Directions of VINS Under Special Motions, Tech. rep., Dept. of Computer Science and Engineering, University of Minnesota (2016).

[7] Y. Yang, G. Huang, Observability Analysis of Aided INS With Heterogeneous Features of Points, Lines, and Planes, IEEE T-RO 35 (6) (2019) 1399–1418. doi:10.1109/TR0.2019.2927835.

[8] A. Geiger, P. Lenz, R. Urtasun, Are we ready for Autonomous Driving? The KITTI Vision Benchmark Suite, in: CVPR, 2012. URL http://www.cvlibs.net/datasets/kitti/eval_odometry.php

[9] K. Ebadi, L. Bernreiter, H. Biggie, G. Catt, Y. Chang, A. Chatterjee, C. E. Denniston, S.-P. Deschênes, K. Harlow, S. Khattak, L. Nogueira, M. Palieri, P. Petráček, M. Petrlik, A. Reinke, V. Krátký, S. Zhao, A.-a. Agha-mohammadi, K. Alexis, C. Heckman, K. Khosoussi, N. Kottege, B. Morrell, M. Hutter, F. Pauling, F. Pomerleau, M. Saska, S. Scherer, R. Siegwart, J. L. Williams, L. Carlone, Present and Future of SLAM in Extreme Underground Environments, arXiv:2208.01787 [cs] (Aug. 2022). doi:10.48550/arXiv.2208.01787.

[10] V. Walter, N. Staub, A. Franchi, M. Saska, UVDAR System for Visual Relative Localization With Application to Leader-Follower Formations of Multirotor UAVs, IEEE RA-L 4 (3) (2019) 2637–2644. doi:10.1109/LRA.2019.2901683.

[11] F. Schilling, F. Schiano, D. Floreano, Vision-Based Drone Flocking in Outdoor Environments, IEEE RA-L 6 (2) (2021) 2954–2961. doi:10.1109/LRA.2021.3062298.

[12] M. Vrba, M. Saska, Marker-Less Micro Aerial Vehicle Detection and Localization Using Convolutional Neural Networks, IEEE RA-L 5 (2) (2020) 2459–2466. doi:10.1109/LRA.2020.2972819.

[13] R. Ge, M. Lee, V. Radhakrishnan, Y. Zhou, G. Li, G. Loianno, Vision-based Relative Detection and Tracking for Teams of Micro Aerial Vehicles, arXiv (Jul. 2022). doi:10.48550/ARXIV.2207.08301.

[14] K. Guo, X. Li, L. Xie, Ultra-Wideband and Odometry-Based Cooperative Relative Localization With Application to Multi-UAV Formation Control, IEEE T. Cybern. 50 (6) (2020) 2590–2603. doi:10.1109/TCYB.2019.2905570.

[15] Y. Huang, T. Shan, F. Chen, B. Englot, DiSCo-SLAM: Distributed Scan Context-Enabled Multi-Robot LiDAR SLAM With Two-Stage Global-Local Graph Optimization, IEEE RA-L 7 (2) (2022) 1150–1157. doi:10.1109/LRA.2021.3138156.

[16] Y. Chang, K. Ebadi, C. E. Denniston, M. F. Ginting, A. Rosinol, A. Reinke, M. Palieri, J. Shi, A. Chatterjee, B. Morrell, A.-a. Agha-mohammadi, L. Carlone, LAMP 2.0: A Robust Multi-Robot SLAM System for Operation in Challenging Large-Scale Underground Environments, IEEE RA-L 7 (4) (2022) 9175–9182. doi:10.1109/LRA.2022.3191204.

[17] Y. Tian, Y. Chang, F. H. Arias, C. Nieto-Granda, J. P. How, L. Carlone, Kimera-Multi: Robust, Distributed, Dense Metric-Semantic SLAM for Multi-Robot Systems, IEEE T-RO (2022) 1–17doi:10.1109/TR0.2021.3137751.

[18] Y. Jang, C. Oh, Y. Lee, H. J. Kim, Multirobot Collaborative Monocular SLAM Utilizing Rendezvous, IEEE T-RO 37 (5) (2021) 1469–1486. doi:10.1109/TR0.2021.3058502.

[19] R. Dubois, A. Eudes, V. Frémont, Sharing visual-inertial data for collaborative decentralized simultaneous localization and mapping, RAS 148 (2022) 103933. doi:10.1016/j.robot.2021.103933.

[20] J. Gross, M. De Petrillo, J. Beard, H. Nichols, T. Swiger, R. Watson, C. Kirk, C. Kilic, J. Hikes, E. Upton, D. Ross, M. Russell, Y. Gu, C. Griffin, Field-Testing of a UAV-UGV Team for GNSS-Denied Navigation in Subterranean Environments, in: ION GNSS+, 2019, pp. 2112–2124. doi:10.33012/2019.16912.

[21] F. Zhu, Y. Ren, F. Kong, H. Wu, S. Liang, N. Chen, W. Xu, F. Zhang, Decentralized LiDAR-inertial Swarm Odometry, arXiv:2209.06628 [cs]

- (Sep. 2022).
- [22] F. Causa, G. Fasano, Adaptive Cooperative Navigation Strategies for Complex Environments, in: *IEEE PLANS*, 2020, pp. 100–111. doi: 10.1109/PLANS46316.2020.9110125.
- [23] F. Causa, R. Opromolla, G. Fasano, Cooperative navigation and visual tracking with passive ranging for UAV flight in GNSS-challenging environments, in: *ICUAS*, 2021. doi:10.1109/ICUAS51884.2021.9476681.
- [24] T.-M. Nguyen, M. Cao, S. Yuan, Y. Lyu, T. H. Nguyen, L. Xie, VIRAL-Fusion: A Visual-Inertial-Ranging-Lidar Sensor Fusion Approach, *IEEE T-RO* 38 (2) (2022) 958–977. doi:10.1109/TR0.2021.3094157.
- [25] T. H. Nguyen, T.-M. Nguyen, L. Xie, Flexible and Resource-Efficient Multi-Robot Collaborative Visual-Inertial-Range Localization, *IEEE RA-L* 7 (2) (2022) 928–935. doi:10.1109/LRA.2021.3136286.
- [26] T. Ziegler, M. Karrer, P. Schmuck, M. Chli, Distributed Formation Estimation Via Pairwise Distance Measurements, *IEEE RA-L* 6 (2) (2021) 3017–3024. doi:10.1109/LRA.2021.3062347.
- [27] H. Xu, L. Wang, Y. Zhang, K. Qiu, S. Shen, Decentralized Visual-Inertial-UWB Fusion for Relative State Estimation of Aerial Swarm, in: *IEEE ICRA*, 2020. doi:10.1109/ICRA40945.2020.9196944.
- [28] H. Xu, Y. Zhang, B. Zhou, L. Wang, X. Yao, G. Meng, S. Shen, Omniswarm: A Decentralized Omnidirectional Visual-Inertial-UWB State Estimation System for Aerial Swarms, *IEEE T-RO* (2022) 1–21doi: 10.1109/TR0.2022.3182503.
- [29] P. Zhang, G. Chen, Y. Li, W. Dong, Agile Formation Control of Drone Flocking Enhanced With Active Vision-Based Relative Localization, *IEEE RA-L* 7 (3) (2022) 6359–6366. doi:10.1109/LRA.2022.3171096.
- [30] J. P. Queralta, L. Qingqing, F. Schiano, T. Westerlund, VIO-UWB-Based Collaborative Localization and Dense Scene Reconstruction within Heterogeneous Multi-Robot Systems, Tech. Rep. arXiv:2011.00830, arXiv (Apr. 2022). doi:10.48550/arXiv.2011.00830.
- [31] I. Spasojevic, X. Liu, A. Ribeiro, G. J. Pappas, V. Kumar, Active Collaborative Localization in Heterogeneous Robot Teams, arXiv:2305.18193 [cs] (May 2023). doi:10.48550/arXiv:2305.18193.
- [32] H. Yu, W. Zhen, W. Yang, J. Zhang, S. Scherer, Monocular Camera Localization in Prior LiDAR Maps with 2D-3D Line Correspondences, in: *IEEE IROS*, 2020. doi:10.1109/IROS45743.2020.9341690.
- [33] S. Cao, X. Lu, S. Shen, GVINS: Tightly Coupled GNSS-Visual-Inertial Fusion for Smooth and Consistent State Estimation, *IEEE T-RO* 38 (4) (2022) 2004–2021. doi:10.1109/TR0.2021.3133730.
- [34] W. Lee, K. Eickenhoff, P. Geneva, G. Huang, Intermittent GPS-aided VIO: Online Initialization and Calibration, in: *IEEE ICRA*, 2020. doi:10.1109/ICRA40945.2020.9197029.
- [35] K. Eickenhoff, Y. Yang, P. Geneva, G. Huang, Tightly-Coupled Visual-Inertial Localization and 3-D Rigid-Body Target Tracking, *IEEE RA-L* 4 (2) (2019) 1541–1548. doi:10.1109/LRA.2019.2896472.
- [36] K. Eickenhoff, P. Geneva, N. Merrill, G. Huang, Schmidt-EKF-based Visual-Inertial Moving Object Tracking, in: *IEEE ICRA*, 2020. doi:10.1109/ICRA40945.2020.9197352.
- [37] T. Baca, M. Petrlik, M. Vrba, V. Spurny, R. Penicka, D. Hert, M. Saska, The MRS UAV System: Pushing the Frontiers of Reproducible Research, Real-world Deployment, and Education with Autonomous Unmanned Aerial Vehicles, *JINT* 102 (1) (2021) 26. doi:10.1007/s10846-021-01383-5.
- [38] V. Pritzl, M. Vrba, P. Stepan, M. Saska, Cooperative Navigation and Guidance of a Micro-Scale Aerial Vehicle by an Accompanying UAV using 3D LiDAR Relative Localization, in: *ICUAS*, IEEE, 2022.
- [39] M. Vrba, Y. Stasinchuk, T. Báča, V. Spurný, M. Petrlik, D. Heřt, D. Žaitlík, M. Saska, Autonomous capture of agile flying objects using UAVs: The MBZIRC 2020 challenge, *RAS* 149 (2022) 103970. doi:10.1016/j.robot.2021.103970.
- [40] M. Vrba, V. Walter, M. Saska, On Onboard LiDAR-based Flying Object Detection, arXiv:2303.05404 [cs] (Mar. 2023). doi:10.48550/arXiv.2303.05404.
- [41] S. Agarwal, K. Mierle, T. C. S. Team, Ceres Solver (Mar. 2022).
- [42] V. Pritzl, M. Vrba, C. Tortorici, R. Ashour, M. Saska, Adaptive estimation of uav altitude in complex indoor environments using degraded and time-delayed measurements with time-varying uncertainties, *RAS* 160 (2023) 104315. doi:https://doi.org/10.1016/j.robot.2022.104315.
- [43] J. Zhang, S. Singh, LOAM: Lidar Odometry and Mapping in Real-time, in: *RSS*, 2014, pp. 109–111. doi:10.15607/RSS.2014.X.007.
- [44] T. Qin, P. Li, S. Shen, VINS-Mono: A Robust and Versatile Monocular Visual-Inertial State Estimator, *IEEE T-RO* 34 (4) (2018) 1004–1020. doi:10.1109/TR0.2018.2853729.
- [45] D. Hert, T. Baca, P. Petracek, V. Kratky, V. Spurny, M. Petrlik, V. Matous, D. Zaitlik, P. Stoudek, V. Walter, P. Stepan, J. Horyna, V. Pritzl, G. Silano, D. Bonilla Licea, P. Stibinger, R. Penicka, T. Nascimento, M. Saska, MRS Modular UAV Hardware Platforms for Supporting Research in Real-World Outdoor and Indoor Environments, in: *ICUAS*, IEEE, 2022.
- [46] D. Hert, T. Baca, P. Petracek, V. Kratky, R. Penicka, V. Spurny, M. Petrlik, M. Vrba, D. Zaitlik, P. Stoudek, V. Walter, P. Stepan, J. Horyna, V. Pritzl, M. Sramek, A. Ahmad, G. Silano, D. B. Licea, P. Stibinger, T. Nascimento, M. Saska, MRS Drone: A Modular Platform for Real-World Deployment of Aerial Multi-Robot Systems, arXiv:2306.07229 [cs] (Jun. 2023). doi:10.48550/arXiv.2306.07229.
- [47] Z. Zhang, D. Scaramuzza, A Tutorial on Quantitative Trajectory Evaluation for Visual-Inertial Odometry, in: *IEEE IROS*, 2018. doi:10.1109/IROS.2018.8593941.
- [48] P. Geneva, K. Eickenhoff, W. Lee, Y. Yang, G. Huang, OpenVINS: A Research Platform for Visual-Inertial Estimation, in: *IEEE ICRA*, 2020. doi:10.1109/ICRA40945.2020.9196524.